ChemComm

RSCPublishing

COMMUNICATION

Probing Battery Chemistry with Liquid Cell Electron Energy Loss Spectroscopy

Raymond R. Unocic,[a*] Loïc Baggetto,[b] Gabriel M. Veith,[b] Kinga A. Unocic,[b] Robert L. Sacci,[b] Nancy J. Dudney,[b] Karren L. More [a]

Received ooth January 2012,

Electron energy loss spectroscopy (EELS) was used to determine the chemistry and oxidation states of $LiMn_2O_4$ and $Li_4Ti_5O_{12}$ thin film battery electrodes confined within liquid cells used for *in situ* scanning/transmission electron microscopy (S/TEM). Using the $L_{2,3}$ white-line intensity ratio method we determine the oxidation state of Mn and Ti in a liquid electrolyte solvent and discuss experimental parameters that influence measurement sensitivity.

In situ liquid S/TEM is a characterization technique that enables the direct imaging and microanalysis of dynamic chemical processes occurring within a liquid environment at high spatial resolution.[1] Using "closed-form" liquid cells, new insights have been gained regarding the mechanism(s) of nanoparticle nucleation and growth,[2-4] complex electron beam induced radiolysis,[5,6] structural imaging of biological structures,[7] and the dynamics of electrochemical processes.[8,9] There is a strong interest in using this method for *in situ* electrochemical S/TEM (*in situ* ec-S/TEM) investigations of nanoscale battery chemistry. Recent studies have focused on using S/TEM to directly visualize formation of the solid electrolyte interphase (SEI)[10-12] and to identify structural changes in battery electrodes during lithiation and delithiation processes,[13-15] but not on the analytical chemistry aspect. The challenge for studying evolving electrochemical processes in battery materials is identifying and quantifying chemical species and oxidation states *in operando*. Holtz et al. used energy filtered TEM (EFTEM) spectroscopic imaging to track lithiation/delithiation kinetics in $LiFePO_4$ under constant current cycling.[14] Furthermore, Sacci et al. determined the chemical composition of SEI compounds and Li electrodeposits following electrochemical cycling using EELS.

The use of electron energy loss spectroscopy (EELS) and energy dispersive spectroscopy (EDS), during the course of liquid cell experiments can provide new insight into the complex chemical changes that occur during chemical and electrochemical redox reactions. The primary concern for performing EELS through liquid cells is directly related to thickness effects and their influence on the detectability limit for inelastically scattered electrons during ionization. Multiple scattering events occur when the electron beam is transmitted through all the components of the liquid cell (SiN_x membranes, liquid layer, and material of interest), which causes a significant decrease in the signal-to-noise ratio (SNR) as a function of increasing fluid layer thickness. Decreasing SNR obscures the low-loss and core-loss ionization edge signals needed for proper chemical analysis.[16,17] There are geometrical limitations for X-ray detection during EDS analysis; the *in situ* TEM holder and silicon microchip devices block X-rays generated within the liquid cell from reaching the EDS detector.[18,19] Modification of the *in situ* TEM holder (sidewall and cover-lid thickness) and the silicon microchip (silicon support thickness and etch pit dimensions) can circumvent this problem.[18] Specific to Li-ion battery chemistry, EELS has the advantage over EDS in light element detection (e.g. Li), which is of particular interest for tracking Li-ion battery chemistries. Furthermore, EELS yields additional analytical information such as the electronic structure and oxidation state of the chemical species.

In this communication, we demonstrate the acquisition of EELS data through a liquid layer and quantitatively identify the chemistry and oxidation state of Mn and Ti in two prototypical Li-transition metal oxide electrode materials $LiMn_2O_4$ (cathode) and $Li_4Ti_5O_{12}$ (anode), confined within a battery solvent, dimethyl carbonate (DMC), in a liquid cell holder for *in situ* microscopy.

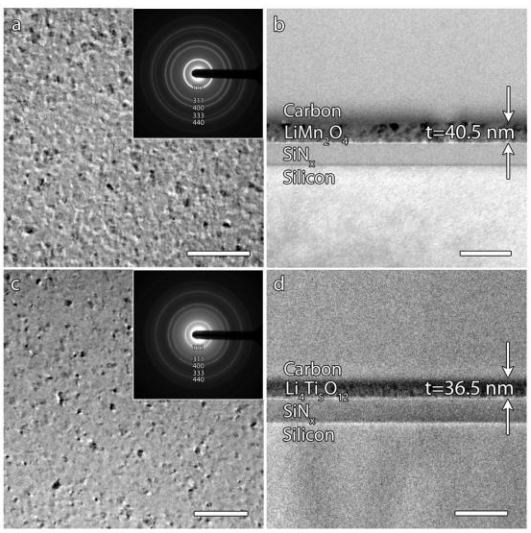

Fig. 1. Plan-view and cross-sectional bright-field TEM images of RF magnetron sputtered thin films deposited directly on the SiN_x membrane of the liquid cell microchip device. TEM images in a-d reveal the nanocrystalline nature and uniform thickness of the sputtered films. (a-b) $LiMn_2O_4$ and (c-d) $Li_4Ti_5O_{12}$. Inset selected area electron diffraction ring patterns are indexed as the spinel structure for both thin films. All scale bars are 100 nm.

Radio frequency (RF) magnetron sputtering was used to deposit thin films of $LiMn_2O_4$ and $Li_4Ti_5O_{12}$, directly on the surface of 50 nm thick SiN_x membranes, which were subsequently annealed. The nanocrystalline grains of the post-annealed thin films are shown in plan-view bright-field TEM images in **Fig. 1a,c** for $LiMn_2O_4$ and $Li_4Ti_5O_{12}$, respectively along with corresponding selected area diffraction ring patterns (inset) that index consistent with spinel crystal structure for both $LiMn_2O_4$ and $Li_4Ti_5O_{12}$. The film thicknesses were 40.5 and 36.5 nm for the $LiMn_2O_4$ and $Li_4Ti_5O_{12}$ films, respectively, as measured from focused ion beam (FIB)-prepared TEM-cross sections (**Fig. 1b,d**). Thin, continuous films were advantageous for the present liquid cell EELS studies, as opposed to nanoparticles, since particle motion induced by Columbic interactions[20] or Brownian motion[21] in the liquid cell is non-existent.

The *in situ* liquid microscopy and EELS experiments were performed using a Hitachi HF-3300 S/TEM (operated at 300kV) equipped with a Gatan Quantum GIF Model 963 with DualEELS™ capabilities, allowing for the simultaneous acquisition of low-loss and core-loss EEL spectra.[22] All EEL spectra were collected with a dispersion of 0.25 eV/channel. The silicon microchips, with the annealed films, were assembled into a liquid cell. Further details for thin film deposition conditions and liquid cell assembly is presented in the electronic supplementary information (ESI) section **(Fig. S1 in ESI**†). The simultaneous acquisition of low-loss and core-loss spectra is beneficial for *in situ* liquid cell EELS measurements since the zero loss peak (ZLP) in the low-loss EEL spectra can be used to remove plural scattering effects from core-loss EEL spectra such that quantitative information regarding the electronic structure and oxidation state can be ascertained. [23] **Fig. 2** shows the low-loss and core-loss EEL spectra of the $LiMn_2O_4$ (**Fig. 2a**) and $Li_4Ti_5O_{12}$ (**Fig. 2b**) thin films, acquired with and without (dry condition) electrolyte. The liquid used here, anhydrous DMC, is a commonly used solvent that comprises up to 70% of a commercial-grade liquid organic battery electrolytes. Commonly used battery salts (e.g. $LiPF_6$, $LiBF_4$, or $LiClO_4$) were not added to the solvent due to the tendency for chemical reduction by solvated electrons, which are generated during electron beam induced radiolysis.[24]

There are several characteristic features present in the EELS data shown in **Fig. 2**. First, there is a noticeable increase in the plasmon peak in the low-loss region of the EEL spectra from the silicon nitride peak at ~24 eV[23], which is due to an increase in total cell thickness due to DMC being present within the liquid cell. Second, the core-loss ionization edges of the Mn $L_{2,3}$-edge and O K-edge in $LiMn_2O_4$ and of the Ti $L_{2,3}$-edge and O K-edge in $Li_4Ti_5O_{12}$ are clearly distinguishable even when there is an increase in total thickness due to DMC in the liquid cell. The N K-edge peak at 401 eV is from the SiN_x membrane. According to Holtz et al., chemical identification from core-loss EELS is limited to 2-3 times the inelastic mean free path (IMFP).[16] Anything greater than this would cause the signal to be obscured by plural scattering events, thereby decreasing SNR. From the low-loss EELS data, the thickness (t) can be determined by the inelastic mean free path (IMFP) (t/λ) approximation, which is defined by the peak intensity ratio between the incident electrons in the ZLP and the unscattered electrons in the first plasmon peak.[25] The t/λ for the $LiMn_2O_4$ between two SiN_x membranes is 0.92 (dry condition) and is 1.42 when DMC is present the liquid cell. Similarly, t/λ for $Li_4Ti_5O_{12}$ is 0.82 (without DMC) and 1.12 (with DMC). With increasing fluid layer thickness (defined by using a 500 nm spacer chip), t/λ becomes larger and it then becomes impossible to quantify core-loss EELS. (Refer to **Fig. S2** in **ESI**†). Note that the presence of DMC in the liquid cell was confirmed by the thickness increase from the low-loss EELS characterization and also by increasing the electron dose until gas bubbles are observed as result of radiolysis (Refer to **Fig. S3** in **ESI**†).

The EELS core-loss ionization edges can be used for chemical identification of Mn and Ti present in the liquid cell; however, additional quantitative information can also be extracted from the data. The valence state and electronic structure of the 3d transition metal (TM) oxides (Mn and Ti), is often evaluated through quantitative analysis of the $L_{2,3}$ ionization edge. For instance, EELS has been used to probe the oxidation state changes of Li-TM battery electrodes following electrochemical charge/discharge cycling.[26,27] The characteristic sharp features of the $L_{2,3}$ white-lines originate from the electronic transition from $2p_{3/2}$ and $2p_{1/2}$ states to unoccupied 3d states. Analysis of the white-line intensity ratio $I(L_3)/I(L_2)$, can be used to determine the oxidation state of the TM cation.[28]

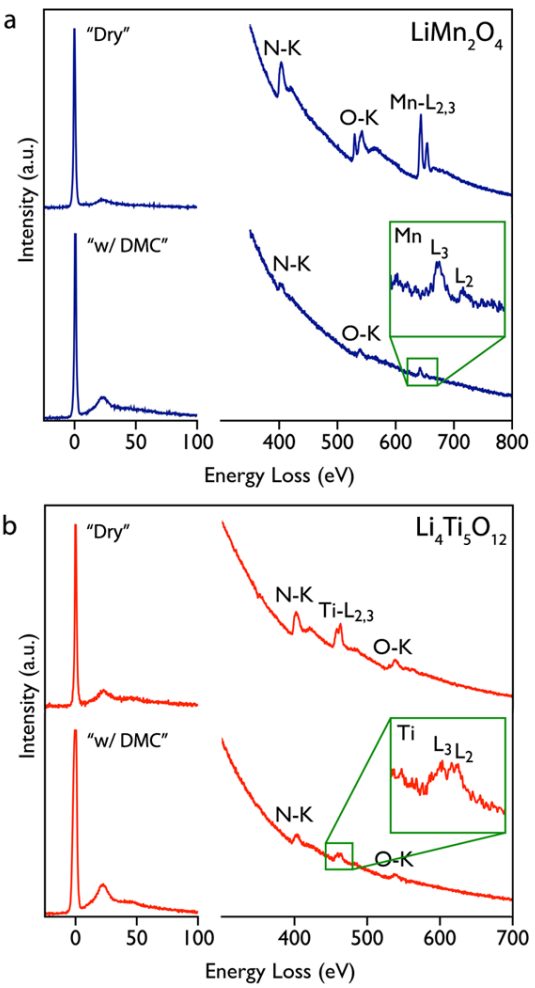

Fig. 2. Experimental low-loss and core-loss EEL spectra of RF magnetron sputtered and annealed a) $LiMn_2O_4$ and b) $Li_4Ti_5O_{12}$ thin films within the liquid cell. Data aquired from the "dry" cell (top-curves) and with anhydrous DMC solvent (lower curves).

The Mn valence state was determine by first performing a Fourier-ratio deconvolution and background subtraction to remove plural scattering affects from the low-loss and core-loss EEL spectra which are presented in **Fig. 3**. For the annealed $LiMn_2O_4$ thin film characterized "dry" between two SiN membranes (no DMC), the characteristic ionization edges corresponding to the N K-edge (at

401 eV), the O K-edge (at 532 eV), and Mn $L_{2,3}$-edges are clearly observed. (**Fig. 3a**) Due to the combination of $LiMn_2O_4$ film thickness, SiN_x thickness, and EELS acquisition parameters used, the O K-edge (532 eV) and characteristic Mn $L_{2,3}$ white-lines of the L_3 (642 eV) and L_2 (652.75 eV) are clearly distinguishable. (**Fig. 3a**) With DMC present in the liquid cell the ionization edges are still identifiable, albeit with a lower SNR. Furthermore, it is apparent that the O K-edge pre-peak is no longer present and there are chemical shifts in energy for the O K-edge peak (shifts 1.5 eV to 538 eV) and the Mn $L_{2,3}$-edge (shifts to 641.25 eV for L_3 and 652.50 eV for L_2). (**Fig. 3b**) The combination of the chemical shift in the Mn $L_{2,3}$ edge and loss of the O K-edge pre-peak is indicative of a lower oxidation state change when DMC is present in the cell. This could be due to a beam induced electrochemical delithation or loss of oxygen (**Fig. 3b**).

Different methods can be used to extract the white-line intensity values to determine the TM oxidation state through the white-line intensity ratio method.[28] A curve fitting method is used here, where the intensity of the L_3 and L_2 edges were obtained from the deconvoluted and background subtracted EEL spectra using a step function that subtracts the continuum intensity.[28,29] The L_3/L_2 white-line intensity ratios for the dry $LiMn_2O_4$ and the DMC-filled liquid cell, were 2.0 and 2.5, respectively. By comparing these values to EELS measurements in standard compounds,[28] it is conclude that the oxidation state of Mn is in the mixed $Mn^{3+/4+}$ state for the dry $LiMn_2O_4$ and shifts towards a Mn^{3+} state when DMC is present in the liquid cell. The loss in the O K-edge pre-peak, shift of the Mn $L_{2,3}$-edge and change in oxidation state suggests that $LiMn_2O_4$ can be prone to electron beam induced chemical lithiation during liquid cell EELS measurements.

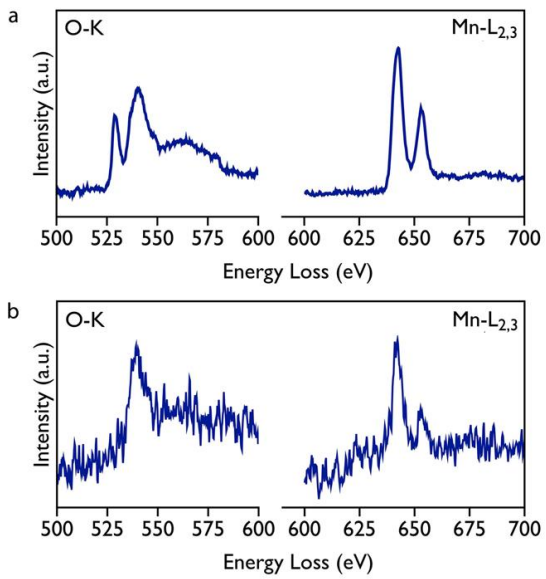

Fig. 3. $LiMn_2O_4$ EEL spectra of the O-K edge and Mn $L_{2,3}$-edge a) between two SiN_x membranes (dry) and b) in the liquid cell filled with DMC. EEL spectra were background subtracted and Fourier-ratio deconvoluted.

A similar approach, was used to analyze the EELS data from the $Li_4Ti_5O_{12}$ thin films. The background subtracted and Fourier-log deconvoluted EEL spectra are shown in **Fig. 4**. The Ti L-edge white-lines exhibits the characteristic splitting into the L_3 and L_2 ionization edges for both the dry $Li_4Ti_5O_{12}$ and DMC filled $Li_4Ti_5O_{12}$ liquid cells. The L_3 and L_2 peaks at 454 and 460 eV for the $Li_4Ti_5O_{12}$ When $Li_4Ti_5O_{12}$ is immersed within DMC, the Ti-$L_{2,3}$ edge is still distinguishable. Although the SNR is low, there are four distinct peaks observed, corresponding to the t_{2g}-e_g splitting of the L_3 and L_2 lines, that are observed of which typical for a Ti^{4+} oxidation state for both conditions. [30,31] It does not appear that $Li_4Ti_5O_{12}$ is sensitive to electron beam induced decomposition. Unlike the EELS data for $LiMn_2O_4$.

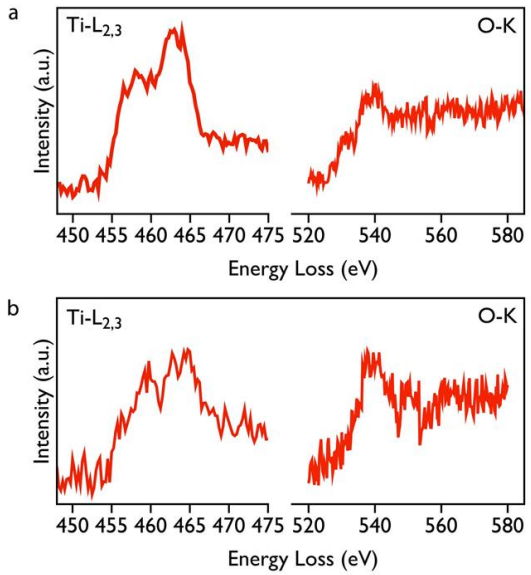

Fig. 4. $Li_4Ti_5O_{12}$ EEL spectra from the O-K edge and Ti $L_{2,3}$-edge a) "dry" and b) in the liquid cell filled with DMC. EEL spectra were background subtracted and Fourier-ratio deconvoluted.

It is important to understand the influence of the electron beam on EELS oxidation state measurements within the liquid cell. For this reason, X-ray photoelectron spectroscopy (XPS) data were collected from the $LiMn_2O_4$ and $Li_4Ti_5O_{12}$ thin films deposited on the SiN_x membranes to determine the oxidation states of Mn and Ti for comparison with the measurements from *in situ* EELS experiments (**Fig. 5**). The Mn 3s split peaks, i.e. ^7S at ~83 eV and ^5S at ~88 eV, are presented in **Fig. 5a**. This core level exhibits splitting between the 3s peaks that is closely related to the oxidation state of Mn and does not suffer from incommensurate charging. For Mn^{3+} the split is present around 5.4 eV, while for Mn^{4+} the split is present around 4.5 eV.[32,33] For the $LiMn_2O_4$ thin film used in this study the split separation measured ~5.1 eV, which is consistent with a mixture of Mn^{3+} and Mn^{4+} as expected for $LiMn_2O_4$ spinel and is consistent with the EELS data reported earlier for the "dry" sample.

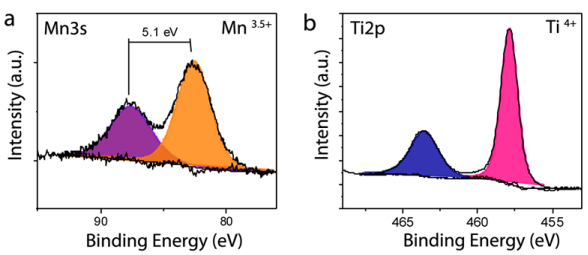

Fig. 5. High-resolution XPS spectra for a) Mn 3s from $LiMn_2O_4$ and b) Ti 2p) for $Li_4Ti_5O_{12}$ thin film materials. Assignments are indicated on the figures.

Moreover, the Mn 3p core level data (**Fig. S3** in **ESI**†) further supports the presence of mixture of about 50% Mn^{3+} and 50% Mn^{4+} cations within the spinel structure, again as expected. The XPS data collected for the $Li_4Ti_5O_{12}$ shows the presence of a single Ti species with a binding energy around 458 eV (**Fig. 5b**). This binding energy is consistent with the presence of Ti^{4+} as expected for $Li_4Ti_5O_{12}$.[34] More systematic studies are needed to throughly study the complex effects of electron beam induced radiolysis on inducing on oxidation state changes during liquid cell studies.

In summary, EELS results from the liquid cell microscopy demonstrate the ability to obtain quantitative chemical information from battery electrode materials during *in situ* ec-S/TEM, experimentation, *in operando*. We have shown that the oxidation state of TMs in thin film battery electrodes can be directly determined using the white-line intensity ratio method even when the materials are fully immersed in a battery electrolyte solvent. These results have important implications for future *in situ* ec-S/TEM experiments, with an achievable goal to use "closed-form" *in situ* electrochemical liquid cells to cycle battery materials within organic battery electrolytes, track electrochemical redox processes and structural changes during electrochemical cycling. Understanding the evolution of battery materials at the nanoscale can lead to an improved understanding of electrode degradation mechanisms for a wide range of electrochemical energy storage and conversion systems.

In situ TEM technique development was supported by the Office of Energy Efficiency and Renewable Energy, Vehicle Technologies Program, U.S. Department of Energy (DOE) (R.R.U., K.A.U., and K.L.M). Thin film RF magnetron sputtering and XPS supported by the Division of Materials Sciences and Engineering Division, Office of Basic Energy Sciences, U.S. DOE (L.B. and G.M.V) and by the Fluid Interface Reactions Structures and Transport (FIRST) Center, an Energy Frontier Research Center funded by the Office of Basic Energy Sciences, U.S. DOE (R.L.S. and N.J.D.). Microscopy conducted as part of a user proposal at ORNL's Center for Nanophase Materials Sciences (CNMS), which is a DOE Science User Facility.

[a] Center for Nanophase Materials Sciences, Oak Ridge National Laboratory, Oak Ridge, TN, USA. E-mail: unocicrr@ornl.gov
[b] Materials Science and Technology Division, Oak Ridge National Laboratory, Oak Ridge, TN, USA.
† Electronic Supplementary Information (ESI) available: Experimental details. See DOI: 10.1039/c000000x/

Notes and references

1. N. de Jonge and F. M. Ross, *Nature Nanotechnology*, 2011, **6**, 695–704.
2. H.-G. Liao, K. Niu, and H. Zheng, *Chemical Communications*, 2013, **49**, 11720.
3. T. J. Woehl, J. E. Evans, I. Arslan, W. D. Ristenpart, and N. D. Browning, *ACS Nano*, 2012, **6**, 8599–8610.
4. T. J. Woehl, C. Park, J. E. Evans, I. Arslan, W. D. Ristenpart, and N. D. Browning, *Nano Letters*, 2014, **14**, 373–378.
5. N. M. Schneider, M. M. Norton, B. J. Mendel, J. M. Grogan, F. M. Ross, and H. H. Bau, *J. Phys. Chem. C*, 2014, **118**, 22373–22382.
6. J. M. Grogan, N. M. Schneider, F. M. Ross, and H. H. Bau, *Nano Letters*, 2014, **14**, 359–364.
7. N. de Jonge, D. B. Peckys, G. Kremers, and W. Piston, *Proceedings of the National Academy of Sciences*, 2009, **106**, 2159–2164.
8. M. J. Williamson, R. M. Tromp, P. M. Vereecken, R. Hull, and F. M. Ross, *Nature Materials*, 2003, **2**, 532–536.
9. E. R. White, S. B. Singer, V. Augustyn, W. A. Hubbard, M. Mecklenburg, B. Dunn, and B. C. Regan, *ACS Nano*, 2012, **6**, 6308–6317.
10. R. L. Sacci, N. J. Dudney, K. L. More, L. R. Parent, I. Arslan, N. D. Browning, and R. R. Unocic, *Chemical Communications*, 2014, **50**, 2104.
11. Z. Zeng, W.-I. Liang, H.-G. Liao, H. L. Xin, Y.-H. Chu, and H. Zheng, *Nano Letters*, 2014, **14**, 1745–1750.
12. R. R. Unocic, X.-G. Sun, R. L. Sacci, L. A. Adamczyk, D. H. Alsem, S. Dai, N. J. Dudney, and K. L. More, *Microscopy and Microanalysis*, 2014, **20**, 1029–1037.
13. M. Gu, L. R. Parent, B. L. Mehdi, R. R. Unocic, M. T. McDowell, R. L. Sacci, W. Xu, J. G. Connell, P. Xu, P. Abellan, X. Chen, Y. Zhang, D. E. Perea, J. E. Evans, L. J. Lauhon, J.-G. Zhang, J. Liu, N. D. Browning, Y. Cui, I. Arslan, and C.-M. Wang, *Nano Letters*, 2013, **13**, 6106–6112.
14. M. E. Holtz, Y. Yu, D. Gunceler, J. Gao, R. Sundararaman, K. A. Schwarz, T. A. Arias, H. D. Abruña, and D. A. Muller, *Nano Letters*, 2014, **14**, 1453–1459.
15. K. W. Noh and S. J. Dillon, *Scripta Materialia*, 2013, **69**, 658–661.
16. M. E. Holtz, Y. Yu, J. Gao, H. D. Abruña, and D. A. Muller, *Microscopy and Microanalysis*, 2013, **19**, 1027–1035.
17. K. L. Jungjohann, J. E. Evans, J. A. Aguiar, I. Arslan, and N. D. Browning, *Microscopy and Microanalysis*, 2012, **18**, 621–627.
18. N. J. Zaluzec, M. G. Burke, S. J. Haigh, and M. A. Kulzick, *Microscopy and Microanalysis*, 2014, **20**, 323–329.
19. E. A. Lewis, S. J. Haigh, T. J. A. Slater, Z. He, M. A. Kulzick, M. G. Burke, and N. J. Zaluzec, *Chemical Communications*, 2014, **50**, 10019–10022.
20. E. R. White, M. Mecklenburg, B. Shevitski, S. B. Singer, and B. C. Regan, *Langmuir*, 2012, **28**, 3695–3698.
21. E. A. Ring and N. de Jonge, *Micron*, 2012, **43**, 1078–1084.
22. A. Gubbens, M. Barfels, C. Trevor, R. Twesten, P. Mooney, P. Thomas, N. Menon, B. Kraus, C. Mao, and B. McGinn, *Ultramicroscopy*, 2015, **110**, 962–970.
23. R. F. Egerton, *Electron Energy-Loss Spectroscopy in the Electron Microscope*, Plenum Press, New York, 2nd edn. 1996.
24. P. Abellan, B. L. Mehdi, L. R. Parent, M. Gu, C. Park, W. Xu, Y. Zhang, I. Arslan, J.-G. Zhang, C.-M. Wang, J. E. Evans, and N. D. Browning, *Nano Letters*, 2014, **14**, 1293–1299.
25. K. Iakoubovskii, K. Mitsuishi, Y. Nakayama, and K. Furuya, *Microsc. Res. Tech.*, 2008, **71**, 626–631.
26. C. R. Fell, D. Qian, K. J. Carroll, M. Chi, J. L. Jones, and Y. S. Meng, *Chem. Mater.*, 2013, **25**, 1621–1629.
27. B. Xu, C. R. Fell, M. Chi, and Y. S. Meng, *Energy Environ. Sci.*, 2011, **4**, 2223.
28. T. Riedl, T. Gemming, and K. Wetzig, *Ultramicroscopy*, 2006, **106**, 284–291.
29. M. Varela, M. Oxley, W. Luo, J. Tao, M. Watanabe, A. Lupini, S. Pantelides, and S. Pennycook, *Phys. Rev. B*, 2009, **79**, 085117.
30. M. Kitta, T. Akita, S. Tanaka, and M. Kohyama, *Journal of Power Sources*, 2013, **237**, 26–32.
31. F. Wang, L. Wu, C. Ma, D. Su, Y. Zhu, and J. Graetz, *Nanotechnology*, 2013, **24**, 424006.
32. A. J. Nelson, J. G. Reynolds, and J. W. Roos, *J. Vac. Sci. Technol. A*, 2000, **18**, 1072.
33. E. Beyreuther, S. Grafström, L. Eng, C. Thiele, and K. Dörr, *Phys. Rev. B*, 2006, **73**, 155425.
34. U. Lafont, D. Carta, G. Mountjoy, A. V. Chadwick, and E. M. Kelder, *J. Phys. Chem. C*, 2010, **114**, 1372–1378.

